


Pilot-wave dynamics: Using dynamic mode decomposition to characterize bifurcations, routes to chaos, and emergent statistics

J. Nathan Kutz ¹, André Nachbin ², Peter J. Baddoo ³, and John W. M. Bush ³

¹*Department of Applied Mathematics and Electrical and Computer Engineering, University of Washington, Seattle, Washington 98195, USA*

²*Department of Mathematical Sciences, Worcester Polytechnic Institute, Worcester, Massachusetts 01742, USA*

³*Department of Mathematics, Massachusetts Institute of Technology, Cambridge, Massachusetts 02139, USA*

 (Received 14 October 2022; revised 7 August 2023; accepted 29 August 2023; published 21 September 2023)

We develop a data-driven characterization of the pilot-wave hydrodynamic system in which a bouncing droplet self-propels along the surface of a vibrating bath. We consider drop motion in a confined one-dimensional geometry and apply the dynamic mode decomposition (DMD) in order to characterize the evolution of the wave field as the bath's vibrational acceleration is increased progressively. Dynamic mode decomposition provides a regression framework for adaptively learning a best-fit linear dynamics model over snapshots of spatiotemporal data. Thus, DMD reduces the complex nonlinear interactions between pilot waves and droplet to a low-dimensional linear superposition of DMD modes characterizing the wave field. In particular, it provides a low-dimensional characterization of the bifurcation structure of the pilot-wave physics, wherein the excitation and recruitment of additional modes in the linear superposition models the bifurcation sequence. This DMD characterization yields a fresh perspective on the bouncing-droplet problem that forges valuable new links with the mathematical machinery of quantum mechanics. Specifically, the analysis shows that as the vibrational acceleration is increased, the pilot-wave field undergoes a series of Hopf bifurcations that ultimately lead to a chaotic wave field. The established relation between the mean pilot-wave field and the droplet statistics allows us to characterize the evolution of the emergent statistics with increased vibrational forcing from the evolution of the pilot-wave field. We thus develop a numerical framework with the same basic structure as quantum mechanics, specifically a wave theory that predicts particle statistics.

DOI: [10.1103/PhysRevE.108.034213](https://doi.org/10.1103/PhysRevE.108.034213)

I. INTRODUCTION

Pilot-wave theories have been developed to describe particle-wave interactions on both the microscopic and macroscopic scales. In quantum mechanics, the double-solution pilot-wave theory of de Broglie [1,2] was proposed in the 1920s on the premise that microscopic particles have an associated internal vibration at the Compton frequency that generates waves. The resonant wave-particle interaction was posited to result in the particle being propelled by its guiding or pilot wave with the de Broglie wavelength, giving rise to statistical behavior consistent with the standard formalism. Hydrodynamic pilot-wave theory [3,4] has been developed to describe the motion of millimetric droplets self-propelling on the surface of a vibrating liquid bath, a system discovered by Couder and Fort in 2005 [5,6]. By virtue of a resonant interaction between the bouncing droplets and the underlying wave field, the droplet is piloted by a quasimonochromatic wave field with the Faraday wavelength. The periodic bouncing of the droplet thus plays the role of the particle vibration in de Broglie's mechanics and the Faraday wavelength that of the de Broglie wavelength [3]. This walking-droplet system is remarkable in that it represents a macroscopic realization of the type of pilot-wave dynamics envisaged by de Broglie and all the more remarkable in that it has yielded a growing list of hydrodynamic quantum analogs [3,4,7]. These include analogs of single-particle diffraction and interference [6,8,9],

orbital quantization [10–14], tunneling [15–17], quantum corrals [18,19], Friedel oscillations [20], spin lattices [21] and long-range correlations in bipartite systems [22–24]. In several of these systems, wavelike statistical forms emerge that are strikingly similar to those arising in their quantum counterparts [18–20]. Hydrodynamic quantum analogs thus suggest that a pilot-wave dynamics of the form engendered in the hydrodynamic system might plausibly underlie quantum statistics [3,4].

The walking-droplet system is complex and strongly nonlinear, being governed by a wave equation for the fluid bath and a trajectory equation for the droplet. The waves are governed by a system of partial differential equations with a nonlocal Fourier operator and a nonlinear forcing induced by the walking droplets. The droplet bounces vertically, and so interacts intermittently with the bath surface, and is propelled by a force proportional to the local slope of the interface during impact. Despite this dynamical complexity and nonlinearity, we proceed by showing that by leveraging the dynamic mode decomposition (DMD), the mean pilot-wave field and droplet statistics can be well characterized by a low-rank linear dynamics.

Specifically, the DMD model shows that linear superposition allows for a reconstruction of the mean wave field, from which we recover the probability density function of the particle. In quantum mechanics, the particle statistics is governed by a linear Schrödinger equation. Here DMD extracts from a

nonlinear system of coupled dynamical equations the linear features of the particle statistics. Dynamic mode decomposition also allows for a characterization of the corresponding bifurcation diagram, specifically the period-doubling route to chaos arising as the vibrational forcing is increased progressively. Our analysis of the walking-droplet system focuses on the dynamics of the waves rather than the particle and provides a simple spatiotemporal modal analysis of the underlying low-dimensional wave interactions that characterize the overall pilot-wave physics and emergent particle statistics.

The feature of the walking-droplet system responsible for the emergent quantum features is path memory [25], which renders the drop dynamics non-Markovian and results from the persistence of the pilot wave on the bath surface. The drop is propelled by its wave field, whose form is prescribed by the droplet's history and environment. The critical control parameter is the bath's vibrational acceleration Γ , which prescribes the bath's proximity to the Faraday threshold Γ_F , above which waves would form even in the absence of the droplet. While Γ is always less than Γ_F in the laboratory, the closer Γ is to Γ_F , the more persistent the waves generated by the droplet, and the longer the path memory. The manner in which the droplet dynamics changes as the vibrational acceleration (or memory) is increased progressively towards the Faraday threshold has been characterized and rationalized for the free droplet [26–28], droplet pairs [29–31], confined rings [32,33], and free rings [34]. Transitions from steady orbital motion to chaotic dynamics have been reported and characterized in a number of settings, including motion in a rotating frame [10–12,35], motion confined by a central force [13,14,36], and motion confined by boundaries [18,19,37]. Rich dynamical properties have been revealed, including period-doubling cascades to chaotic trajectories [11,35,38,39]. The dynamical system aspects of the walking-droplet system have been highlighted in the recent review by Rahman and Blackmore [40].

In characterizing the bifurcation structure of the walking-droplet system, prior work has focused primarily on the droplet dynamics, specifically how the particle trajectory changes with increasing memory. However, for confined walker motion, connections between the mean pilot-wave field and the emergent statistical forms have been both reported [19] and rationalized [37,41]. As the resulting mean pilot wave is expressible in terms of the droplet's statistical behavior, Bush and Oza [4] proposed that it may play a role similar to that of the quantum potential in Bohmian mechanics. While the mean walker dynamics is thus effectively nonlocal, as is Bohmian mechanics, the time-resolved walker dynamics is entirely local. The present work focuses on the bifurcation structure of the pilot wave as the system memory is increased progressively. By leveraging the DMD, the underlying pilot-wave field can be characterized, revealing its own period-doubling cascade to chaos. The analysis provides a spatiotemporal modal analysis of the underlying low-dimensional wave interactions that characterize the overall pilot-wave physics.

Dynamic mode decomposition originated as a modal analysis method in the fluid dynamics community. Introduced as an algorithm by Schmid and Sesterhenn [42,43], it has

rapidly become a commonly used data-driven analysis tool and the standard algorithm to approximate the Koopman operator from data [44]. Specifically, DMD was used to identify dominant spatiotemporal coherent fluid structures from high-dimensional time-series data. The DMD analysis offered an alternative to standard dimensionality reduction methods such as the proper orthogonal decomposition (POD), which highlighted low-rank features in fluid flows using the computationally efficient singular value decomposition (SVD) [45]. The advantage of using DMD over SVD is that the DMD modes are linear combinations of the SVD modes that have a common linear (exponential) behavior in time, given by oscillations at a fixed frequency with growth or decay. Specifically, optimized DMD [46,47] is a regression to solutions of the form

$$\mathbf{x}(t) = \sum_{j=1}^r b_j \boldsymbol{\phi}_j e^{\omega_j t}, \quad (1)$$

where $\mathbf{x}(t)$ is a rank- r approximation to a collection of state space measurements $\mathbf{x}_k = \mathbf{x}(t_k)$ ($k = 1, 2, \dots, n$). The algorithm finds the DMD eigenvalues ω_j , DMD modes $\boldsymbol{\phi}_j$, and their loadings b_j . The ω_j determines the temporal behavior of the system associated with a modal structure $\boldsymbol{\phi}_j$, thus giving a highly interpretable representation of the dynamics. Such a regression can also be learned from time-series data [48]. Dynamic mode decomposition may be thought of as a combination of the SVD and POD in space with the Fourier transform in time, combining the strengths of each approach [49,50].

Dynamic mode decomposition also provides a natural mathematical connection with pilot-wave hydrodynamics. Specifically, the emergent steady-state statistics of the walking droplets have been shown in certain instances to be comparable to solutions of the time-independent Schrödinger equation of quantum mechanics [4,18,19]. The time-dependent Schrödinger equation takes the general form

$$i\psi_t = -\psi_{xx} + V(x)\psi, \quad (2)$$

where $\psi(x, t)$ is the wave function, $V(x)$ is a potential, and the coefficients have been normalized to unity. The solution of the Schrödinger equation is given by a linear superposition of modes, each of which has a characteristic oscillation frequency. In quantum mechanics, these frequencies are the energy levels of the quantum system. Although the interpretation of these solutions is quite different from that of the fluidic system under consideration, the representation of the systems in terms of a linear superposition of modes oscillating at characteristic frequencies is the same. Thus, despite the complexity of the fluidic system, its approximate DMD solution generates the canonical Sturm-Liouville solution form. Specifically, the state-space variable $\mathbf{x}(t)$ (1) is the vectorized version of the Schrödinger wave field $\psi(x, t)$. The general solution to the discretized Schrödinger equation is given by the DMD approximation (1) where the modes and frequencies are determined by regression in order to model the complex nonlinear and nonlocal interactions between wave field and droplet. In this case, the DMD modes and eigenvalues correspond to the eigenstates and their corresponding energy levels, respectively, of the quantum system. Thus, DMD provides not

only a valuable approximation method but a regression to the solution form that is standard in quantum mechanics.

II. PILOT-WAVE PHYSICS

The walking-droplet system is modeled theoretically through a trajectory equation for the droplet and a partial differential equation that describes the spatiotemporal dynamics of the accompanying waves [26–28]. The wave model may be obtained from an asymptotic simplification of the linear free-surface Navier-Stokes equations [51]. The Helmholtz decomposition of the velocity field yields, in the weakly viscous regime, an irrotational velocity potential perturbed by a weak shearing component, arising through the stream function. The pilot wave along the undisturbed free surface $z = 0$ is expressed through a weakly diffusive Bernoulli law as well as a weakly diffusive kinematic condition, as detailed below. The velocity potential is denoted by $\phi(x, z, t)$, where we note that in the formulation that follows, the dynamics are constrained to the x - z plane. The velocity field components in the bulk of the fluid are given by $(u, v) = \nabla\phi$. The wave elevation is denoted by $\eta(x, t)$. The fluid parameters are the fluid density ρ , the surface tension σ , and the kinematic viscosity ν . In the reference frame of the fluid bath, which oscillates at frequency ω_0 , gravity takes the form $g(t) = g[1 + \Gamma \sin(\omega_0 t)]$. The free-surface wave equations are given by [16,51]

$$\frac{\partial\phi}{\partial t}(x, 0, t) = -g(t)\eta + \frac{\sigma}{\rho}\eta_{xx} + 2\nu\phi_{xx} - \frac{1}{\rho}P_d[x - X(t)], \quad (3)$$

$$\frac{\partial\eta}{\partial t}(x, t) = \mathcal{O}_{\text{DtN}}[\phi] + 2\nu\eta_{xx}. \quad (4)$$

The diffusive terms, in both the Bernoulli law and the kinematic condition, are the leading-order terms from the vortical component of the Helmholtz decomposition. The presence of the droplet is felt through the pressure term P_d , centered at the droplet's position $X(t)$, which acts as a wave maker. This pressure term is compactly supported in space, over the droplet's diameter, and is discontinuous in time, being activated periodically at each bounce. The velocity potential satisfies Laplace's equation, which enables one to define the Dirichlet-to-Neumann operator that maps the Dirichlet data $\phi(x, 0, t)$ onto the free surface's normal speed, at time t :

$$\mathcal{O}_{\text{DtN}}[\phi] = \phi_z(x, 0, t). \quad (5)$$

The operator \mathcal{O}_{DtN} is defined as a Fourier integral operator and is computed in a straightforward manner using a conformal mapping and the fast Fourier transform [16].

To complete the wave-particle model, the above wave system is coupled to the droplet's horizontal trajectory equation [27]

$$m\frac{d^2X}{dt^2} + cF(t)\frac{dX}{dt} = -F(t)\frac{\partial\eta}{\partial x}(X(t), t). \quad (6)$$

The drop is propelled by the wave force, which is proportional to the local gradient of the wave field, and resisted by a linear drag. The magnitude of the propulsive wave force transmitted during the contact time, here prescribed as $T_c = T_F/4$, where T_F is the Faraday period, is denoted by $F(t)$. This

time-dependent coefficient also appears in the drag term, since drag is also imparted during impact. Further modeling details can be found elsewhere [16,51].

The evolution of the PDE model is shown in Fig. 1. As the forcing amplitude is increased, the walking-droplet system undergoes a bifurcation sequence. For low-amplitude forcing $\Gamma = 4.8$, the droplet bounces in place in the middle of the well [Fig. 1(a)]. As the forcing amplitude is increased, the droplet begins to oscillate periodically in the well [Fig. 1(b)]. A further increase of Γ generates larger oscillations until eventually period doubling occurs, which is detailed in Sec. V. The dynamics of the droplet can also be plotted in phase space using the droplet position, denoted by X , and the droplet speed, denoted by $V = \dot{X}$. Figure 2 shows the underlying attractors associated with the dynamics illustrated in Fig. 1. Increasing Γ leads to a chaotic motion of the droplet, as further detailed in Fig. 3. The center of oscillation varies in a chaotic fashion. As will be detailed in Sec. V, the bifurcation sequence exhibits a period-doubling bifurcation sequence to chaos, which is canonical for damped-driven systems [52–55].

The corresponding pilot-wave dynamics of Fig. 2 is highlighted in Fig. 4. As Γ takes on the values 4.8, 5.0, 5.3, and 5.4, the pilot wave evolves from a steady field to a periodic wave to a doubly periodic wave to spatiotemporal chaos. In what follows we will illustrate that the spatiotemporal dynamics can be completely characterized by the DMD. Indeed, DMD exploits the low-rank structure of the wave field as shown in Fig. 5. Truncation of the SVD modes is typically done in a heuristic fashion. Often, a prescribed variance, such as 99%, is sought for the truncation criterion. Here the truncated modes selected are prescribed by cross validation of the reconstruction error. Thus, modes aside from the dominant zero background mode are selected as complex conjugate pairs until the reconstruction error is only marginally improved by the inclusion of additional modes. Ultimately, the smallest number of modes capable of accurately reconstructing the solution is sought. Thus, in Fig. 5 the numbers of modes used as Γ takes on the values 4.8, 5.0, 5.3, and 5.4 are one, three, five, and nine, respectively. The addition of more modes in any of these dynamical regimes has little impact on the reconstruction error.

III. DYNAMIC MODE DECOMPOSITION

The DMD algorithm can be best understood from the so-called exact DMD [56], which is simply a least-square fitting procedure. Specifically, the exact DMD algorithm seeks a best-fit linear operator \mathbf{A} that approximately advances the state of a system, $\mathbf{x} \in \mathbb{R}^n$, forward in time according to the linear dynamical system

$$\mathbf{x}_{k+1} = \mathbf{A}\mathbf{x}_k, \quad (7)$$

where $\mathbf{x}_k = \mathbf{x}(k\Delta t)$, with Δt denoting a fixed time step that is small enough to resolve the highest frequencies in the dynamics. Thus, the operator \mathbf{A} is an approximation of the Koopman operator \mathcal{K} restricted to a measurement subspace spanned by direct measurements of the state \mathbf{x} [44,57]. One can work directly with the measured variables \mathbf{x} or construct alternative observables via a number of different methods [57]. Time-delay embeddings, for instance, often offer an improved

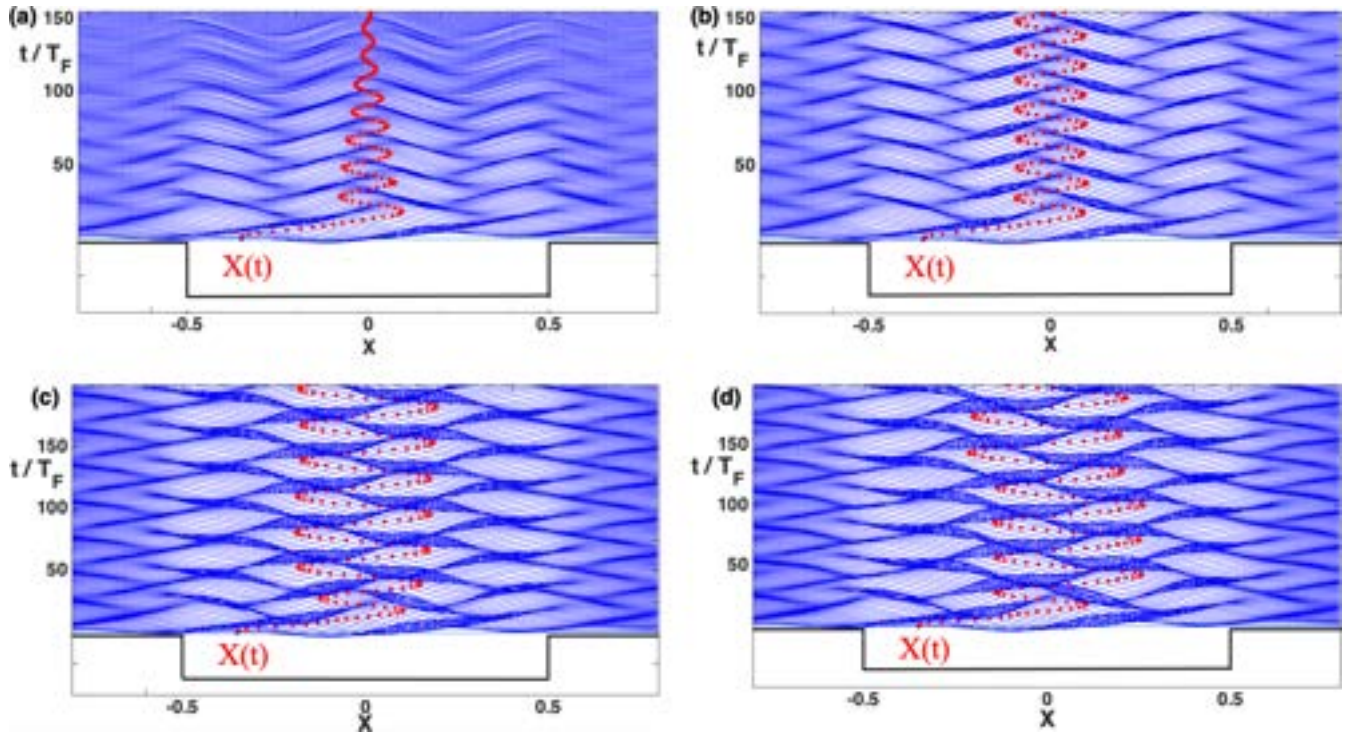


FIG. 1. Wave-droplet dynamics over 150 Faraday periods in a cavity of width 1 cm. The vibrational forcing takes the values (a) $\Gamma = 4.8$, (b) $\Gamma = 5.0$, (c) $\Gamma = 5.3$, and (d) $\Gamma = 5.4$. For this geometry the Faraday threshold is approximately $\Gamma_F = 6.15$. All other parameters are kept unchanged, including the droplet’s initial position at $X = -0.35$. The wave field $\eta(x, t)$ is denoted by blue while the horizontal droplet position $X(t)$ is indicated by red.

characterization of nonlinear systems [58–61]. However, the fluidic wave-particle system considered here is well characterized by a linear DMD model from measurements of the

wave field alone. Thus there is no need to seek improved observables for the system.

Bagheri [62] first highlighted that DMD is particularly sensitive to the effects of noisy data, with systematic biases introduced to the eigenvalue distribution [63–66]. The optimized DMD algorithm of Askham and Kutz [46], which uses a variable projection method for nonlinear least squares to

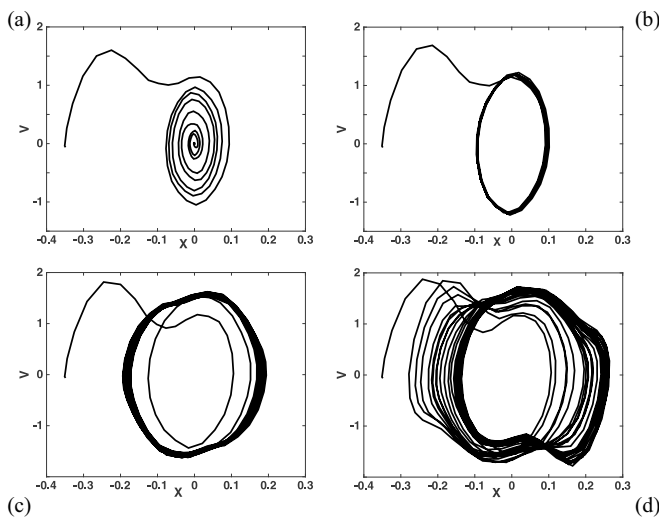


FIG. 2. Phase-space dynamics. The droplet position is denoted by X and the droplet speed by $V = \dot{X}$. Panels correspond to extensions of the sequences illustrated in Fig. 1, for which (a) $\Gamma = 4.8$, (b) $\Gamma = 5.0$, (c) $\Gamma = 5.3$, and (d) $\Gamma = 5.4$, and the initial particle position $X(0) = -0.35$. The total time for the simulations is (a) and (b) $t = 4000T_F$ and (c) and (d) $t = 8000T_F$.

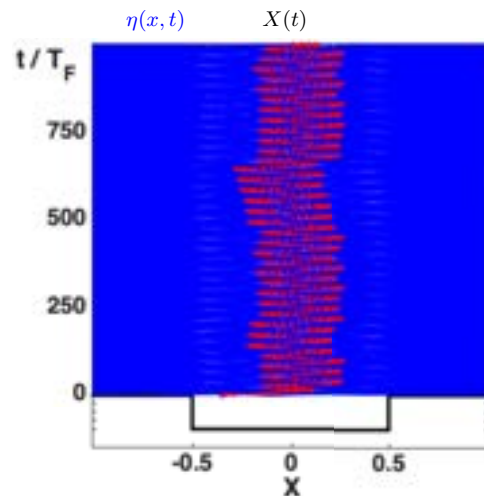


FIG. 3. Simulation of particle-wave dynamics with $\Gamma = 5.4$, displayed over a longer time interval than in Fig. 1(d). The wave field $\eta(x, t)$ is denoted by blue while the droplet position $X(t)$ is indicated by red.

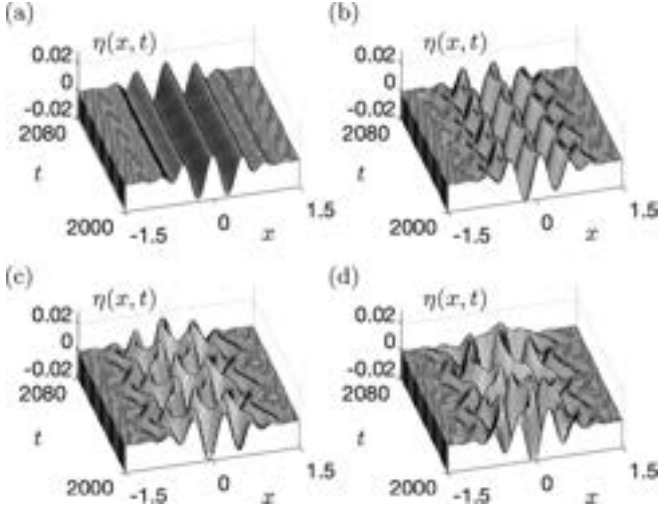


FIG. 4. Pilot-wave dynamics corresponding to Fig. 1, where Γ takes on the values (a) 4.8, (b) 5.0, (c) 5.3, and (d) 5.4. The pilot-wave field is shown for $t \in [2000, 2080]$ after the droplet behavior has settled into its long time dynamics, as illustrated in Figs. 1 and 2.

compute the DMD for unevenly timed samples, provides the best performance of any algorithm currently available. This is because it directly solves the exponential fitting problem of DMD. Consider the data matrix

$$\mathbf{X} = \begin{bmatrix} | & | & & | \\ \mathbf{x}(t_1) & \mathbf{x}(t_2) & \cdots & \mathbf{x}(t_m) \\ | & | & & | \end{bmatrix}. \quad (8)$$

The optimized DMD algorithm directly solves the exponential fitting problem in order to produce the matrix decomposition.

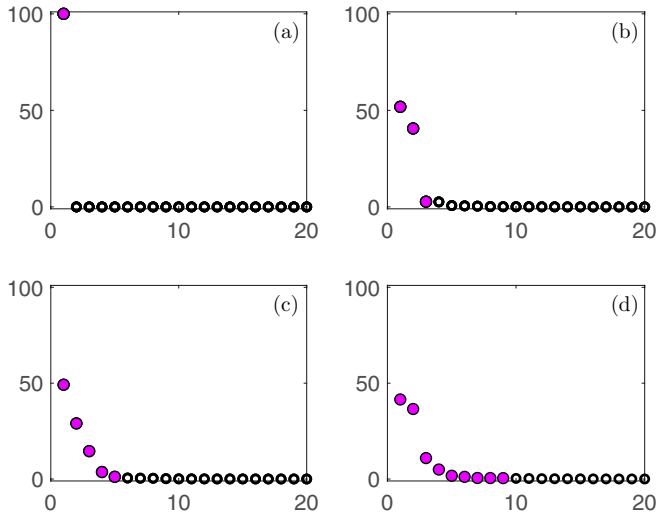


FIG. 5. Low-rank structure of the pilot-wave dynamics corresponding to Fig. 4, where Γ takes on the values (a) 4.8, (b) 5.0, (c) 5.3, and (d) 5.4. The singular value decomposition shows the percentage of variance in each SVD mode, i.e., the j th mode variance is equal to $100\sigma_j / \sum \sigma_k$. The variance of only the first 20 modes is shown, with the magenta modes depicting the number of modes required for accurate DMD reconstruction.

Thus, the data matrix \mathbf{X} may be reconstructed as

$$\begin{aligned} \mathbf{X} &\approx \Phi \text{diag}(\mathbf{b})\mathbf{T}(\omega) \\ &= \begin{bmatrix} | & & | \\ \phi_1 & \cdots & \phi_r \\ | & & | \end{bmatrix} \begin{bmatrix} b_1 & & \\ & \ddots & \\ & & b_r \end{bmatrix} \begin{bmatrix} e^{\omega_1 t_1} & \cdots & e^{\omega_1 t_m} \\ \vdots & \ddots & \vdots \\ e^{\omega_r t_1} & \cdots & e^{\omega_r t_m} \end{bmatrix}. \quad (9) \end{aligned}$$

The variable projection method for this approximation [46] determines the parameters of the matrix components. Thus the optimization is formulated as

$$\arg \min_{\omega, \Phi_b} \|\mathbf{X} - \Phi_b \mathbf{T}(\omega)\|_F, \quad (10)$$

where $\Phi_b = \Phi \text{diag}(\mathbf{b})$. Thus optimized DMD provides a direct approximation to the solution (1), which is a regression to the form of the modal solution expansion to the vectorized Schrödinger equation. This has been shown to provide a superior decomposition due to its ability to optimally suppress bias and handle snapshots collected at arbitrary times. Dynamic mode decomposition approximations do not constrain the DMD eigenvalue to the imaginary axis. However, the optimized DMD regression can be modified to fit eigenvalues on the imaginary axis or to constrain eigenvalues to the left half plane for stability [46]. These constraints are not enforced in what follows. Moreover, with statistical bagging, the BOP-DMD algorithm (bagging, optimized DMD) also provides robust models with uncertainty quantification in the presence of noise, corruption, and outliers [47]. Physically motivated constraints can also be embedded into the DMD architecture [67], further enhancing the algorithm. The disadvantage of optimized DMD is that one must solve a nonlinear optimization problem, which can fail to converge.

IV. INFERRING PARTICLE STATISTICS FROM WAVE DYNAMICS

Durey *et al.* [37] deduced a simple relation between the mean pilot-wave field and the droplet statistics for walker motion in a statistically steady state, either periodic or ergodic. For a particle moving in a bounded region (for example, when constrained by a central force), the mean wave field $\bar{\eta}$ may be expressed as the convolution of the wave field of a stationary bouncer η_B and the droplet's histogram $\mu(\mathbf{x})$, normalized to have total mass one. Note that in this instance, where boundary effects are negligible, η_B is independent of the droplet position but does depend on the system memory. For a domain with variable bottom topography relevant for the cavity considered here, the result was generalized by Durey *et al.* [41] through incorporation of the spatial dependence of the bouncer wave field resulting from the influence of boundaries. The convolution is thus generalized to an integral operator, where the kernel $\eta_G(x, y)$ is given by the wave field of a bouncer located at position y . In this case, the statistics of the particle and its pilot wave are related by (see Eq. 3.2 in [41])

$$\bar{\eta}(x) = \int_{-\infty}^{\infty} \eta_G(x, y) \mu(y) dy, \quad (11)$$

where $\bar{\eta}(x) = \lim_{N \rightarrow \infty} \frac{1}{N} \sum_{k=1}^N \eta(x, t_k)$ is the time-averaged wave field and $t_k = kT_F$. We note that numerical verification

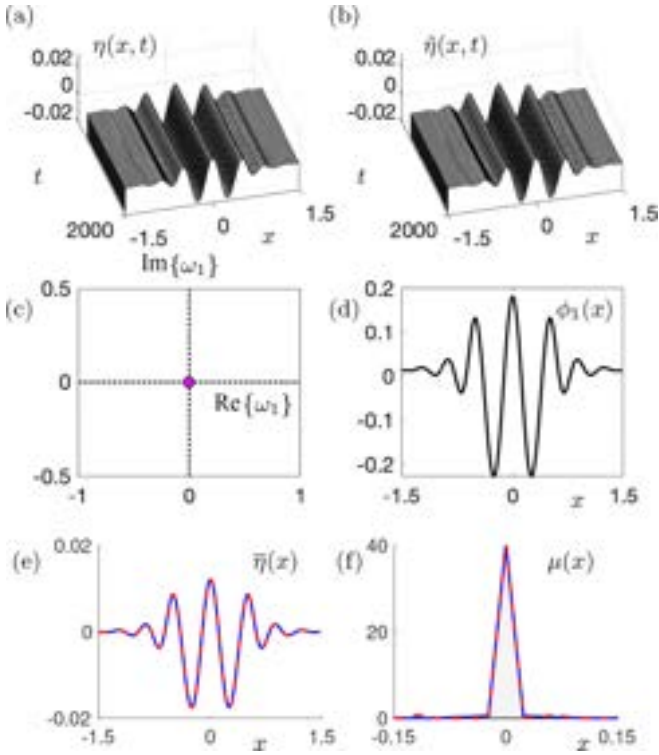


FIG. 6. Pilot-wave dynamics for the lowest forcing value considered, $\Gamma = 4.8$. The simulation was run for 4000 Faraday periods (or droplet bounces). Figure 5 shows that a rank-1 decomposition is sufficient to model the steady-state wave dynamics. (a) Full PDE evolution. (b) One-mode DMD approximation. (c) DMD eigenvalue. (d) DMD eigenfunction used for reconstruction of the spatiotemporal dynamics. Note that the DMD eigenvalue is at the origin, which is consistent with the steady-state behavior in this parameter regime. (e) Time-averaged pilot-wave field calculated directly (blue solid line) and deduced from the measured particle probability distribution via (11) (red dashed line). (f) Particle probability distribution as computed via particle tracking (blue solid line) and inferred from the mean pilot wave by inverting Eq. (11) (red dashed line).

of (11) was not presented in [41]. In Figs. 6(e), 7(e), 8(e), and 9(e) we compare the time-averaged wave field, computed directly from the numerical simulations, with that predicted by the expression (11). The agreement is excellent, even for the cases where the phase-space orbits indicate complex cycles. To be explicit, the time-averaged wave field is the DMD mode associated with the zero eigenvalue. Moreover, DMD shows that the inferred particle statistics are expressible in terms of a very few eigenmodes of the respective spectrum.

We proceed by exploring the relation (11) in a novel fashion. Inverting the integral operator allows us to infer particle statistics from the mean wave field (as may be viewed as an effective potential) computed over the time interval of interest. The particle statistics is thus obtained with no specific knowledge of the particle dynamics, a step that evokes quantum mechanics. Numerical aspects of the operator inversion are presented in the Appendix. Figures 6(f), 7(f), 8(f), and 9(f) compare the particle's probability density function, as deduced directly from particle tracking, with that produced by inverting equation (11). The agreement between the two is

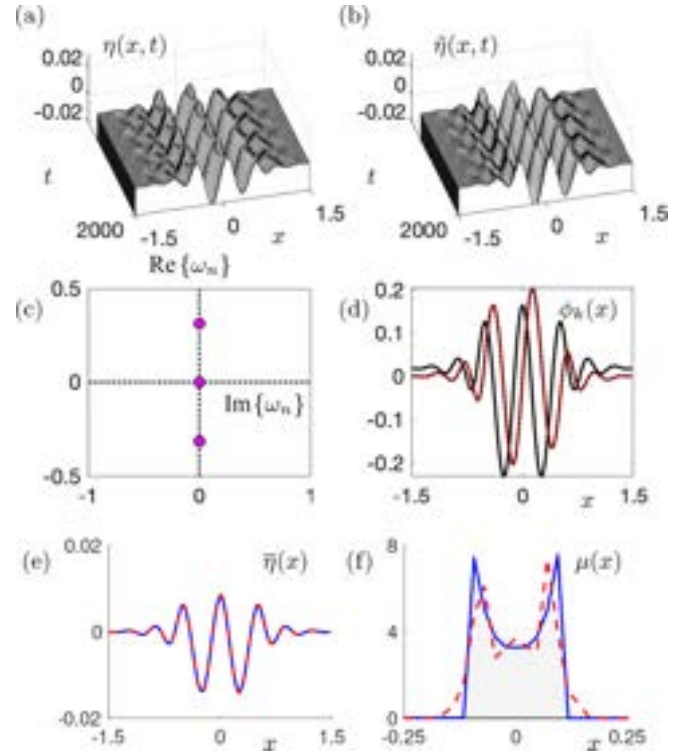


FIG. 7. Pilot-wave dynamics for $\Gamma = 5.0$. The simulation was run for 4000 Faraday periods. Figure 5 shows that a rank-3 decomposition is adequate to model the spatiotemporal periodic behavior observed. (a) Full PDE evolution. (b) Three-mode DMD approximation. (c) DMD eigenvalues. (d) DMD eigenfunctions used for reconstruction of the spatiotemporal dynamics. (The black dotted line shows the steady-state background mode of Fig. 6.) Note that the DMD eigenvalues are manifest in complex conjugate pairings typical of an underlying Hopf bifurcation. (e) Time-averaged pilot-wave field (blue solid line) and that deduced from the measured particle probability distribution via (11) (red dashed line). (f) Particle probability distribution as computed via particle tracking (blue solid line) and inferred from the mean pilot wave by inverting Eq. (11) (red dashed line).

satisfactory in all cases. Thus, without having recorded the particle dynamics, we obtain a good approximation to the particle statistics from the time-averaged wave field $\bar{\eta}$.

V. DYNAMICS AND BIFURCATIONS

The optimized DMD algorithm is used on the wave data shown in Fig. 4 using a low-rank truncation suggested by Fig. 5. Specifically, as the forcing parameter Γ takes on the values 4.8, 5.0, 5.3, and 5.4, the low-rank structure is well captured by one, three, five, and nine modes, respectively. As will be detailed below, the number of modes used was dictated by the minimum number of modes required to reproduce an accurate representation of the dynamics.

Figures 6–9 illustrate the dynamics as the dynamics transitions from the lowest value of $\Gamma = 4.8$ to the highest value of $\Gamma = 5.4$. Each of the four figures have six panels which illustrate the characteristics dynamics as the forcing parameter Γ takes on the values 4.8, 5.0, 5.3, and 5.4. Figures 6(a), 7(a), 8(a), and 9(a) show the wave dynamics

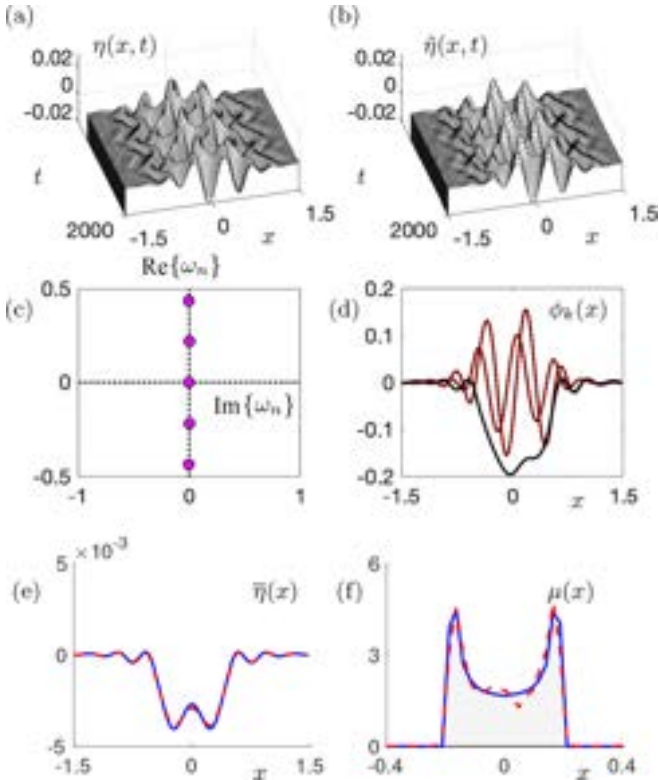


FIG. 8. Pilot-wave dynamics for $\Gamma = 5.3$. The simulation was run of 8000 Faraday periods. Figure 5 shows that a rank-5 decomposition is adequate to model the spatiotemporal periodic behavior observed. (a) Full PDE evolution. (b) Five-mode DMD approximation. (c) DMD eigenvalues. (d) DMD eigenfunctions used for reconstruction of the spatiotemporal wave dynamics. (The black dotted line shows the steady-state background mode.) Note that the DMD eigenvalues appear in complex conjugate pairs whose frequencies are approximately harmonic, leading to the secondary period-doubling dynamics manifest in the pilot-wave field. (e) Time-averaged pilot-wave field as computed directly (blue solid line) and deduced from the particle probability distribution via (11) (red dashed line). (f) Particle probability distribution as computed via particle tracking (blue solid line) and inferred from the mean pilot wave by inverting Eq. (11) (red dashed line).

after the decay of all transients in the system (Fig. 2). Recall that the wave field has been strobed to remove oscillations at the Faraday frequency. Figures 6(a), 7(a), 8(a), and 9(a) show the evolution of the full PDE simulations, while Figs. 6(b), 7(b), 8(b), and 9(b) show the low-rank DMD reconstruction. The accompanying DMD eigenvalue and DMD eigenfunction are shown in Figs. 6(c), 7(c), 8(c), and 9(c) and Figs. 6(d), 7(d), 8(d), and 9(d), respectively. Note that the eigenvalue at the origin captures a stationary behavior, while the complex conjugate pairs of eigenfunctions capture the periodic dynamics of the wave field. Figures 6(e), 7(e), 8(e), and 9(e) show the mean pilot-wave field (blue solid line) and that deduced from Durey’s convolution theorem [37,41] (red dashed line). Figures 6(f), 7(f), 8(f), and 9(f) show the particle probability distribution as computed directly from particle tracking (blue solid line) and inferred from the mean pilot wave by inverting Eq. (11) (red dashed line).

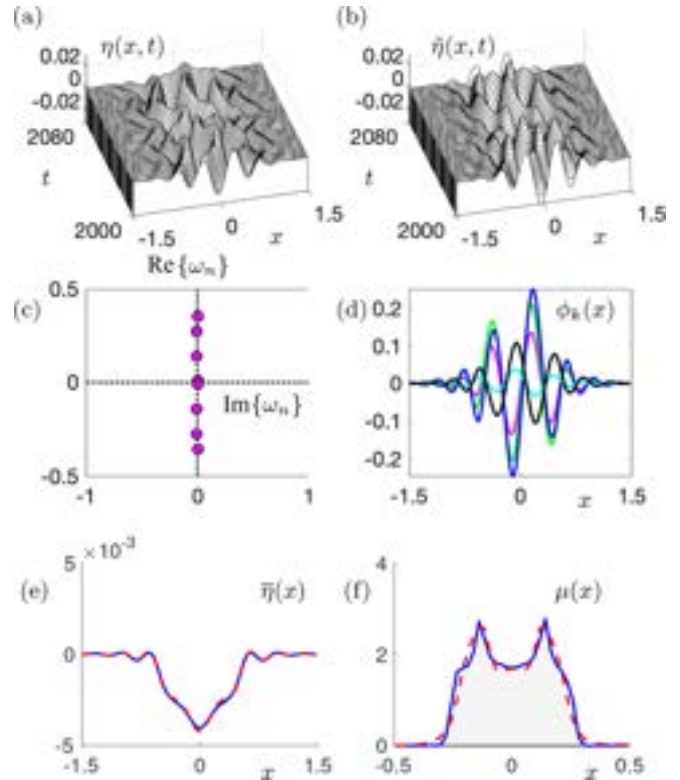


FIG. 9. Pilot-wave dynamics for the highest forcing value considered, $\Gamma = 5.4$. The simulation was run for 8000 Faraday periods. Figure 5 shows that a rank-9 decomposition is adequate to model the spatiotemporal chaotic behavior observed. (a) Full PDE evolution. (b) Nine-mode DMD approximation. (c) DMD eigenvalues. (d) DMD eigenfunctions used for reconstruction of the spatiotemporal wave dynamics. (The black dotted line shows the steady-state background mode as computed over the limited time interval shown.) Note that the DMD eigenvalues appear in complex conjugate pairings whose frequencies are incommensurate, which is responsible for the relatively complex dynamics. (e) Time-averaged pilot-wave field computed directly (blue solid line) and that deduced from the measured particle probability distribution via (11) (red dashed line). (f) Particle probability distribution as computed via particle tracking (blue solid line) and inferred from the mean pilot wave by inverting Eq. (11) (red dashed line).

Note that as the bifurcation sequence progresses, a period-doubling bifurcation is observed with the generation of harmonics in the DMD spectra (see Figs. 7 and 8). Specifically, we note that the simulations reported were executed just beyond the bifurcation point at which the period doubling is expected to hold exactly; thus, the frequencies in normalized units are 0.17 and 0.32. The period doubling of the pilot wave corroborates the well-characterized period-doubling behavior of the droplet itself as reported in a number of settings involving orbital dynamics [11,35,38,39]. Once the forcing is sufficiently large, the complex conjugate pairs are no longer harmonic, thus producing the observed spatiotemporal chaos. The overall period-doubling route to chaos is thus evident in the simulations. Moreover, as the forcing becomes sufficiently large, the DMD spectrum generated from the optimized DMD regression produces eigenvalues with small but nonzero real

TABLE I. Comparison of the quantum description of a particle in a one-dimensional well and the pilot-wave system considered here.

	Quantum mechanics	Pilot-wave hydrodynamics
driving parameter	particle energy	memory parameter γ
waveform	quantum wave function Ψ	Faraday pilot wave $h(x, t)$
statistical inference	Born's rule	integral operator inversion ^a

^aFrom [41].

parts in the spectrum of (9). This is expected since the regression is not forced to find eigenvalues constrained to the imaginary axis.

The evolution from Fig. 6 to Fig. 9 shows the underlying onset of instability in this pilot-wave hydrodynamic system. This period doubling is canonical for damped-driven systems, from optics to combustion [52–55]. The optimized DMD algorithm provides a data-driven algorithm that provides a regression to the exponential solution form (1) commonly used to model physical systems, from quantum mechanics to electrodynamics. Thus, DMD provides interpretable models and a clear quantification of the evolution of the pilot-wave field accompanying the droplet dynamics.

VI. CONCLUSION

Particle-wave interactions arise throughout the physical sciences. The specific example considered here of the pilot-wave hydrodynamic system has generated significant interest due to its connection to quantum mechanics. Indeed, pilot-wave hydrodynamics has provided a compelling example of well-resolved classical particle-wave interactions producing quantumlike statistics. To date, the particle dynamics has received the bulk of the mathematical attention, and the emergent statistics have been seen as a compelling feature of the system that is not always simply rationalized. Here we have instead focused on the evolution of the pilot wave and the inference of system statistics. By leveraging the dynamic mode decomposition, the pilot-wave dynamics has been shown to execute a period-doubling cascade typically observed in damped-driven systems ranging from detonation waves to mode-locked lasers. Dynamic mode decomposition provides a low-rank approximation of the pilot-wave dynamics into a set of spatial modes with associated temporal frequencies. The regression framework of DMD provides a best-fit linear dynamics model over snapshots of spatiotemporal data. The DMD characterization of the wave field yields a different perspective on the walking-droplet problem that forges valuable links with quantum mechanics. In particular, it naturally decomposes the wave field into modes of the form prevalent in standard quantum theory.

Our analysis has shown that as the vibrational acceleration is increased progressively, the pilot wave undergoes a series of Hopf bifurcations in which new modes at approximately harmonic frequencies emerge, culminating in a period-doubling cascade to spatiotemporal chaos. Such a period-doubling route to chaos is a canonical feature of damped-driven systems, which can be related to the logistic map in which the

same canonical bifurcation structure is evident. The simplicity of the logistic map belies the rich and complicated behavior that it captures [68]. Given the diversity of models capable of producing this same bifurcation structure [52–55], it is highly suggestive that energy balance considerations alone can dictate the overall physics in such damped-driven systems. Specifically, the gain and loss dynamics in the hydrodynamic pilot-wave system produce a mapping between the driving energy input and the damping losses that generate a period-doubling cascade [39].

Our study has demonstrated how classical pilot-wave dynamics, like quantum mechanics, may yield predictions for the statistical behavior of particles on the basis of a wave theory. The map between the quantum and classical pilot-wave descriptions of particle motion in a one-dimensional well is presented in Table I. In quantum mechanics, the relevant wave form is the wave function Ψ , while in our system it is the pilot wave. In quantum mechanics, the number of modes excited depends on the particle energy. In our pilot-wave system, the system memory plays an analogous role. Note that as either of these control parameters is increased progressively, a discrete set of new wave modes is introduced. In quantum mechanics, the waves correspond to the complex wave function Ψ ; in our system, the waves correspond to the pilot wave. In quantum mechanics, the statistical behavior of the particles is prescribed by Born's rule: The density of states is prescribed by the square of the wave function $|\Psi|^2$. In our pilot-wave system, the density of states is inferred from the mean pilot wave via the operator inversion suggested by the theorem of Durey *et al.* [41].

In summary, the DMD algorithm is a regression to exponential solutions of the form (1). In quantum mechanics, the solution (1) is typically constructed using analytical (or semianalytical) techniques where appropriate boundary and matching conditions are imposed for a given potential. Since Schrödinger's equation is linear, such an eigendecomposition provides a set of linear basis modes which can be superimposed to express any solution. Dynamic mode decomposition is a regression directly to the solution form (1), using variable projection to compute amplitudes b_j , modes ϕ_j , and frequencies ω_j of the exponential solutions directly from data. In the quantum scenario, one must know the potential in order to construct the solutions. In contrast, DMD can be used in a completely data-driven manner without knowledge of the underlying potential. Thus DMD is advantageous for scenarios where an unknown effective potential determines the underlying dynamics. Moreover, it provides the best approximation of the form (1) even when the underlying dynamics is nonlinear, such as is the case with the hydrodynamic analog system.

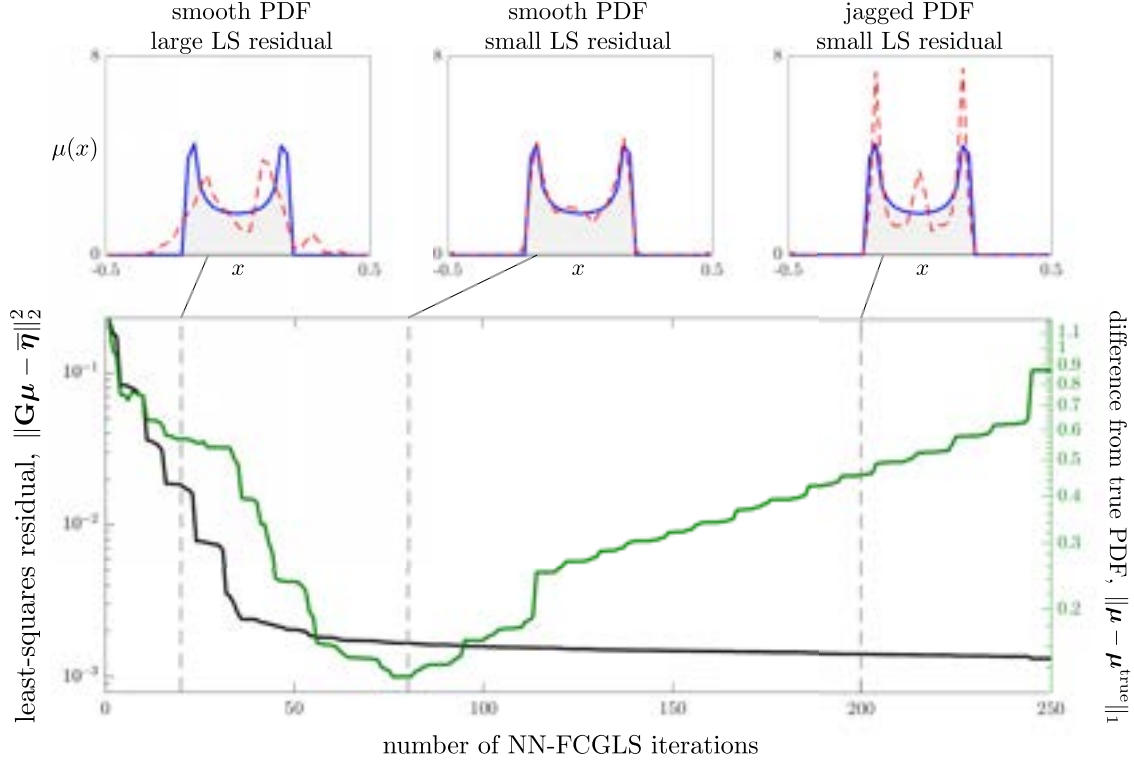


FIG. 10. Effects of terminating the NN-FCGLS algorithm at different numbers of iterations. If the algorithm is terminated too early then the least-squares residual in (A2) is large; if the algorithm is terminated too late then the ensuing PDF is too jagged. The plotted PDFs in the top row are computed with 20, 80, and 200 iterations, respectively.

ACKNOWLEDGMENTS

P.J.B. and J.N.K. acknowledge support from the National Science Foundation AI Institute in Dynamic Systems (Grant No. 2112085). J.W.M.B. gratefully acknowledges support from the National Science Foundation through Grant No. CMMI-2154151. A.N. acknowledges support from CNPq under (PQ1D) Grant No. 307078/2021-3 and FAPERJ Cientistas do Nosso Estado Project No. E-26/201.156/2021.

APPENDIX: CALCULATING THE PARTICLE PROBABILITY DENSITY FUNCTION FROM THE AVERAGE WAVE FIELD

In this Appendix we detail the practical steps involved in computing the particle probability density function (PDF) from the average wave field. We use the full time window of the simulated system (3)–(6) to calculate the average wave field and the true PDF. Discretizing (11) on a grid of equispaced points $\{x_1, \dots, x_{128}\}$ produces the system

$$\bar{\eta} = \mathbf{G}\boldsymbol{\mu}, \quad (\text{A1})$$

where $\{\boldsymbol{\mu}\}_i = \mu(x_i)$, $\{\bar{\eta}\}_i = \bar{\eta}(x_i)$, and $\{\mathbf{G}\}_{i,j} = \eta_G(x_i, x_j)$. Our goal is now to find a $\boldsymbol{\mu}$ that solves (A1) for a given Green's function matrix \mathbf{G} and an observed mean wave field $\bar{\eta}$. The wave field is observed over a finite time horizon, so the resulting time average invariably contains noise. As such, the observed average wave differs from the true average wave, so we write

$$\bar{\eta} = \bar{\eta}^{\text{true}} + \boldsymbol{\epsilon},$$

where $\boldsymbol{\epsilon}$ is a vector of noise corresponding to the temporal truncation error. Therefore, we consider a least-squares optimization problem to find the particle histogram: We seek the optimal vector $\boldsymbol{\mu}^*$ defined by

$$\boldsymbol{\mu}^* = \arg \min_{\boldsymbol{\mu}} \|\mathbf{G}\boldsymbol{\mu} - \bar{\eta}\|_2^2. \quad (\text{A2})$$

Additionally, we are only interested in solutions that represent probability density functions. In other words, $\boldsymbol{\mu}^*$ must be non-negative and have unit mass, specifically,

$$\boldsymbol{\mu}^* \geq \mathbf{0}, \quad \|\Delta x \boldsymbol{\mu}^*\|_1 = 1, \quad (\text{A3})$$

where $\Delta x = x_2 - x_1$ is the equispaced quadrature weight. The above constraints effectively regularize the problem (A2) and remove unphysical solutions. However, the matrix \mathbf{G} is ill-conditioned [with condition number $O(10^{10})$], so taking an inverse or repeatedly applying \mathbf{G} can be unreliable. Furthermore, \mathbf{G} has a large approximate null space, so many candidate PDFs produce small residuals in (A2).

We deployed several classical methods [69] to solve the inverse problem in (A2). Ultimately, we found that the non-negative flexible conjugate-gradient least-squares (NN-FCGLS) method of Gazzola and Wiaux [70] provided the most robust results. The NN-FCGLS method is a Krylov subspace method and is implemented in the IR TOOLS package [71]. Although the NN-FCGLS method does not enforce the unit mass constraint, the computed solutions have mass very close to one.

It is important to control the number of iterations executed by the NN-FCGLS method, as illustrated in Fig. 10. Therein,

we plot the least-squares residual ($\|\mathbf{G}\boldsymbol{\mu} - \bar{\boldsymbol{\eta}}\|_2$) and the error between the calculated and the true PDFs ($\|\boldsymbol{\mu} - \boldsymbol{\mu}^{\text{true}}\|_1$) when $\boldsymbol{\mu}$ is calculated after the given number of iterations. In practice, the true PDF is unavailable, so we include the PDF error here only for the sake of illustration. We select the iteration number that produces a PDF satisfying two criteria: It must attain a small residual error in (A2) and it must be sufficiently smooth. Too few iterations can result in large residuals in (A2) and too many iterations result in a jagged (nonsmooth) solution. Since the data are generated from a continuous dynamical system, we can exclude solutions that are not smooth. Chapter 2 of [69] suggests alternative criteria for selecting the number of iterations of conjugate gradient methods.

Figure 10 shows three candidate PDFs that we evaluate according to these two criteria. The first PDF is produced after

20 NN-FCGLS iterations. It is smooth, but has a low least-squares residual, so we discard it. The third PDF is produced after 200 iterations. It has a small residual, but is jagged, so we discard it. The second PDF is produced after 80 iterations. It has a small residual and is smooth. Accordingly, we select this PDF as our solution $\boldsymbol{\mu}^*$. The green solid curve in Fig. 10 confirms that this is a good choice of PDF. Indeed, selecting anywhere between 70 and 100 NN-FCGLS iterations would have produced a satisfactory PDF.

Finally, an advantage of using Krylov methods is that they can be applied when one has access only to a linear operator that evaluates matrix-vector products $\mathbf{G}\mathbf{v}$, as opposed to \mathbf{G} itself. Accordingly, the NN-FCGLS method scales well and will be suitable for higher-dimensional problems, such as a particle in a circular corral [18,41].

- [1] L. de Broglie, Ondes et quanta, *Comptes Rendus* **177**, 507 (1923).
- [2] L. de Broglie, Interpretation of quantum mechanics by the double solution theory, *Ann. Fond. L. de Broglie* **12**, 1 (1987).
- [3] J. W. M. Bush, Pilot-wave hydrodynamics, *Annu. Rev. Fluid Mech.* **47**, 269 (2015).
- [4] J. W. M. Bush and A. U. Oza, Hydrodynamic quantum analogs, *Rep. Prog. Phys.* **84**, 017001 (2020).
- [5] Y. Couder, S. Protiere, E. Fort, and A. Boudaoud, Walking and orbiting droplets, *Nature (London)* **437**, 208 (2005).
- [6] Y. Couder and E. Fort, Single-Particle Diffraction and Interference at a Macroscopic Scale, *Phys. Rev. Lett.* **97**, 154101 (2006).
- [7] J. W. M. Bush, Y. Couder, T. Gilet, P. A. Milewski, and A. Nachbin, Introduction to focus issue on hydrodynamic quantum analogs, *Chaos* **28**, 096001 (2018).
- [8] G. Pucci, P. J. Sáenz, L. M. Faria, and J. W. M. Bush, Non-specular reflection of walking droplets, *J. Fluid Mech.* **804**, R3 (2016).
- [9] C. Ellegaard and M. T. Levinsen, Interaction of wave-driven particles with slit structures, *Phys. Rev. E* **102**, 023115 (2020).
- [10] E. Fort, A. Eddi, J. Moukhtar, A. Boudaoud, and Y. Couder, Path-memory induced quantization of classical orbits, *Proc. Natl. Acad. Sci. USA* **107**, 17515 (2010).
- [11] D. M. Harris and J. W. M. Bush, Drops walking in a rotating frame: From quantized orbits to multimodal statistics, *J. Fluid Mech.* **739**, 444 (2014).
- [12] A. U. Oza, D. M. Harris, R. R. Rosales, and J. W. M. Bush, Pilot-wave dynamics in a rotating frame: On the emergence of orbital quantization, *J. Fluid Mech.* **744**, 404 (2014).
- [13] S. Perrard, M. Labousse, M. Miskin, E. Fort, and Y. Couder, Self-organization into quantized eigenstates of a classical wave-driven particle, *Nat. Commun.* **5**, 3219 (2014).
- [14] M. Labousse, S. Perrard, Y. Couder, and E. Fort, Build-up of macroscopic eigenstates in a memory-based constrained system, *New J. Phys.* **16**, 113027 (2014).
- [15] A. Eddi, E. Fort, F. Moisy, and Y. Couder, Unpredictable Tunneling of a Classical Wave-Particle Association, *Phys. Rev. Lett.* **102**, 240401 (2009).
- [16] A. Nachbin, P. A. Milewski, and J. W. M. Bush, Tunneling with a hydrodynamic pilot-wave model, *Phys. Rev. Fluids* **2**, 034801 (2017).
- [17] L. Tadrst, T. Gilet, P. Schlagheck, and J. W. M. Bush, Predictability in a hydrodynamic pilot-wave system: Resolution of walker tunneling, *Phys. Rev. E* **102**, 013104 (2020).
- [18] D. M. Harris, J. Moukhtar, E. Fort, Y. Couder, and J. W. M. Bush, Wavelike statistics from pilot-wave dynamics in a circular corral, *Phys. Rev. E* **88**, 011001(R) (2013).
- [19] P. J. Sáenz, T. Cristea-Platon, and J. W. M. Bush, Statistical projection effects in a hydrodynamic pilot-wave system, *Nat. Phys.* **14**, 315 (2018).
- [20] P. J. Sáenz, T. Cristea-Platon, and J. W. M. Bush, A hydrodynamic analog of Friedel oscillations, *Sci. Adv.* **6**, 20 (2020).
- [21] P. J. Saenz, G. Pucci, S. E. Turton, A. Goujon, R. R. Rosales, J. Dunkel, and J. W. M. Bush, Emergent order in hydrodynamic spin lattices, *Nature (London)* **596**, 58 (2021).
- [22] A. Nachbin, Walking droplets correlated at a distance, *Chaos* **28**, 096110 (2018).
- [23] K. Papatryfonos, M. Ruelle, C. Bourdiol, A. Nachbin, J. W. M. Bush, and M. Labousse, Hydrodynamic superradiance via wave-mediated cooperative tunneling, *Commun. Phys.* **5**, 142 (2022).
- [24] A. Nachbin, Effect of isolation on two-particle correlations in pilot-wave hydrodynamics, *Phys. Rev. Fluids* **7**, 093604 (2022).
- [25] A. Eddi, E. Sultan, J. Moukhtar, E. Fort, M. Rossi, and Y. Couder, Information stored in Faraday waves: The origin of a path memory, *J. Fluid Mech.* **674**, 433 (2011).
- [26] J. Moláček and J. W. M. Bush, Droplets bouncing on a vibrating fluid bath, *J. Fluid Mech.* **727**, 582 (2013).
- [27] J. Moláček and J. W. M. Bush, Drops walking on a vibrating bath: Towards a hydrodynamic pilot-wave theory, *J. Fluid Mech.* **727**, 612 (2013).
- [28] A. U. Oza, R. R. Rosales, and J. W. M. Bush, A trajectory equation for walking droplets: Hydrodynamic pilot-wave theory, *J. Fluid Mech.* **737**, 552 (2013).
- [29] J. Arbelaiz, A. U. Oza, and J. W. M. Bush, Promenading pairs of walking droplets: Dynamics and stability, *Phys. Rev. Fluids* **3**, 013604 (2018).
- [30] A. U. Oza, E. Siéfert, D. M. Harris, J. Moláček, and J. W. M. Bush, Orbiting pairs of walking droplets: Dynamics and stability, *Phys. Rev. Fluids* **2**, 053601 (2017).
- [31] M. M. P. Couchman, S. E. Turton, and J. W. M. Bush, Bouncing phase variations in pilot-wave hydrodynamics and the stability of droplet pairs, *J. Fluid Mech.* **871**, 212 (2019).

- [32] S. J. Thomson, M. M. P. Couchman, and J. W. M. Bush, Collective vibrations of confined levitating droplets, *Phys. Rev. Fluids* **5**, 083601 (2020).
- [33] S. J. Thomson, M. Durey, and R. R. Rosales, Collective vibrations of a hydrodynamic active lattice, *Proc. R. Soc. A* **476**, 20200155 (2020).
- [34] M. M. P. Couchman and J. W. M. Bush, Free rings of bouncing droplets: Stability and dynamics, *J. Fluid Mech.* **903**, A49 (2020).
- [35] A. U. Oza, Ø. Wind-Willassen, D. M. Harris, R. R. Rosales, and J. W. M. Bush, Pilot-wave hydrodynamics in a rotating frame: Exotic orbits, *Phys. Fluids* **26**, 082101 (2014).
- [36] M. Durey, Bifurcations and chaos in a Lorenz-like pilot-wave system, *Chaos* **30**, 103115 (2020).
- [37] M. Durey, P. A. Milewski, and J. W. M. Bush, Dynamics, emergent statistics and the mean-pilot-wave potential of walking droplets, *Chaos* **28**, 096108 (2018).
- [38] L. D. Tambasco, D. M. Harris, A. U. Oza, R. R. Rosales, and J. W. M. Bush, The onset of chaos in orbital pilot-wave dynamics, *Chaos* **26**, 103107 (2016).
- [39] A. Rahman and J. N. Kutz, Walking droplets as a damped-driven system, *SIAM J. Appl. Dyn. Syst.* **22**, 1219 (2023).
- [40] A. Rahman and D. Blackmore, Walking droplets through the lens of dynamical systems, *Mod. Phys. Lett. B* **34**, 2030009 (2020).
- [41] M. Durey, P. A. Milewski, and Z. Wang, Faraday pilot-wave dynamics in a circular corral, *J. Fluid Mech.* **891**, A3 (2020).
- [42] P. J. Schmid and J. Sesterhenn, in *Proceedings of the 61st Annual Meeting of the APS Division of Fluid Dynamics, San Antonio, 2008* (American Physical Society, Ridge, 2008).
- [43] P. J. Schmid, Dynamic mode decomposition of numerical and experimental data, *J. Fluid Mech.* **656**, 5 (2010).
- [44] C. W. Rowley, I. Mezić, S. Bagheri, P. Schlatter, and D. S. Henningson, Spectral analysis of nonlinear flows, *J. Fluid Mech.* **641**, 115 (2009).
- [45] J. N. Kutz, *Data-Driven Modeling & Scientific Computation: Methods for Complex Systems & Big Data* (Oxford University Press, Oxford, 2013).
- [46] T. Askham and J. N. Kutz, Variable projection methods for an optimized dynamic mode decomposition, *SIAM J. Appl. Dyn. Syst.* **17**, 380 (2018).
- [47] D. Sashidhar and J. N. Kutz, Bagging, optimized dynamic mode decomposition (BOP-DMD) for robust, stable forecasting with spatial and temporal uncertainty-quantification, *Phil. Trans. R. Soc. A* **380**, 20210199 (2022).
- [48] H. Lange, S. L. Brunton, and J. N. Kutz, From Fourier to Koopman: Spectral methods for long-term time series prediction, *J. Mach. Learn. Res.* **22**, 1881 (2021).
- [49] K. K. Chen, J. H. Tu, and C. W. Rowley, Variants of dynamic mode decomposition: Boundary condition, Koopman, and Fourier analyses, *J. Nonlinear Sci.* **22**, 887 (2012).
- [50] J. N. Kutz, S. L. Brunton, B. W. Brunton, and J. L. Proctor, *Dynamic Mode Decomposition: Data-Driven Modeling of Complex Systems* (SIAM, Philadelphia, 2016).
- [51] P. A. Milewski, C. A. Galeano-Rios, A. Nachbin, and J. W. M. Bush, Faraday pilot-wave dynamics: Modelling and computation, *J. Fluid Mech.* **778**, 361 (2015).
- [52] F. Li, P. Kong A. Wai, and J. N. Kutz, Geometrical description of the onset of multi-pulsing in mode-locked laser cavities, *J. Opt. Soc. Am. B* **27**, 2068 (2010).
- [53] K. M. Spaulding, D. H. Yong, A. D. Kim, and J. N. Kutz, Nonlinear dynamics of mode-locking optical fiber ring lasers, *J. Opt. Soc. Am. B* **19**, 1045 (2002).
- [54] E. Ding and J. N. Kutz, Operating regimes, split-step modeling, and the Haus master mode-locking model, *J. Opt. Soc. Am. B* **26**, 2290 (2009).
- [55] J. Koch, M. Kurosaka, C. Knowlen, and J. N. Kutz, Multiscale physics of rotating detonation waves: Autosolitons and modulational instabilities, *Phys. Rev. E* **104**, 024210 (2021).
- [56] J. H. Tu, C. W. Rowley, D. M. Luchtenburg, S. L. Brunton, and J. N. Kutz, On dynamic mode decomposition: Theory and applications, *J. Comput. Dyn.* **1**, 391 (2014).
- [57] S. L. Brunton, M. Budišić, E. Kaiser, and J. N. Kutz, Modern Koopman theory for dynamical systems, *SIAM Rev.* **64**, 229 (2022).
- [58] S. L. Brunton, B. W. Brunton, J. L. Proctor, E. Kaiser, and J. N. Kutz, Chaos as an intermittently forced linear system, *Nat. Commun.* **8**, 19 (2017).
- [59] H. Arbabi and I. Mezić, Ergodic theory dynamic mode decomposition, and computation of spectral properties of the Koopman operator, *SIAM J. Appl. Dyn. Syst.* **16**, 2096 (2017).
- [60] M. Kamb, E. Kaiser, S. L. Brunton, and J. N. Kutz, Time-delay observables for Koopman: Theory and applications, *SIAM J. Appl. Dyn. Syst.* **19**, 886 (2020).
- [61] S. M. Hirsh, S. M. Ichinaga, S. L. Brunton, J. N. Kutz, and B. W. Brunton, Structured time-delay models for dynamical systems with connections to Frenet-Serret frame, Serret frame *Proc. R. Soc. A* **477**, 20210097 (2021).
- [62] S. Bagheri, Effects of weak noise on oscillating flows: Linking quality factor, Floquet modes, and Koopman spectrum, *Phys. Fluids* **26**, 094104 (2014).
- [63] D. Duke, J. Soria, and D. Honnery, An error analysis of the dynamic mode decomposition, *Exp. Fluids* **52**, 529 (2012).
- [64] S. Bagheri, Koopman-mode decomposition of the cylinder wake, *J. Fluid Mech.* **726**, 596 (2013).
- [65] S. T. M. Dawson, M. S. Hemati, M. O. Williams, and C. W. Rowley, Characterizing and correcting for the effect of sensor noise in the dynamic mode decomposition, *Exp. Fluids* **57**, 42 (2016).
- [66] M. S. Hemati, C. W. Rowley, E. A. Deem, and L. N. Cattafesta, De-biasing the dynamic mode decomposition for applied Koopman spectral analysis, *Theor. Comput. Fluid Dyn.* **31**, 349 (2017).
- [67] P. J. Baddoo, B. Herrmann, B. J. McKeon, J. N. Kutz, and S. L. Brunton, Physics-informed dynamic mode decomposition, *Proc. R. Soc. A* **479**, 20220576 (2023).
- [68] R. M. May, Simple mathematical models with very complicated dynamics, *Nature* **261**, 459 (1976).
- [69] J. P. Kaipio and E. Somersalo, *Statistical and Computational Inverse Problems*, Applied Mathematical Sciences Vol. 160 (Springer, New York, 2005).
- [70] S. Gazzola and Y. Wiaux, Fast nonnegative least squares through flexible Krylov subspaces, *SIAM J. Sci. Comput.* **39**, A655 (2017).
- [71] S. Gazzola, P. C. Hansen, and J. G. Nagy, IR Tools: A MATLAB package of iterative regularization methods and large-scale test problems, *Numer. Algor.* **81**, 773 (2019).